Acta Astronautica 206 (2023) 100–113

Contents lists available at ScienceDirect

Acta Astronautica

journal homepage: www.elsevier.com/locate/actaastro

Analysis of spray characteristics of a jet-film injection element based on Voronoi tessellation

Chengming He [a,b], Peng Zhang [c], Zhixia He [a], Lianjie Yue [b,*]

[a] Institute for Energy Research, Jiangsu University, Zhenjiang, 212013, China
[b] Institute of Mechanics, Chinese Academy of Sciences, Beijing, 100190, China
[c] Department of Mechanical Engineering, City University of Hong Kong, Kowloon Tong, Kowloon, 999077, Hong Kong

ARTICLE INFO

Keywords:
Liquid rocket engine
Pintle injector
Spray characteristics
Jet-film injection
Voronoi tessellation

ABSTRACT

The present paper presents a computational study based on a validated Volume-of-Fluid method on the effects of film thickness and film width on spray characteristics for the simplified jet-film injection element with varying mass flow rate conditions. First, the spray characteristics of a typical jet-film collision were analyzed in terms of the spatial distribution of Sauter Mean Diameter and Voronoi tessellation. Both the Voronoi diagram and the Sauter Mean Diameter contour are useful to evaluate the spray characteristics because they show two different aspects of the sprays. Second, the jet-film spray characteristics were analyzed by decreasing either film thickness or film width to change the mass flow rate. The results show that decreasing film width results in approximately insensitive spray angle and improved uniformity of droplet distribution for different throttleable levels. The present computational results verified our design concept that adopting traditional jet-film injection at a large mass flow rate and modified jet-jet injection at a small mass flow rate to maintain good spray performance during the entire throttleable levels.

1. Introduction

The throttleable engines with variable thrust capacities [1,2] are promising and superior for wide-range flight vehicles, for example, the Rocket-based Combined Cycle (RBCC) engine [3], and hypersonic vehicles [4] to improve the maneuverability. The capacity of variable thrust is generally achieved by varying the mass flow rate of propellants, and the pintle injector [5] for injection strategy and combustion is one of the best choices owing to its simple geometric structure, continuous change of mass flow rate, and combustion stability. The most successful engineering application of pintle injectors is the Lunar Module Descent Engine (LMDE) [6] designed and developed by TRW Company [7] in the Apollo 11 lunar landing program of the United States in the 1960s.

The operating principle of pintle injectors [5,8,9] has the main feature that the moveable pintle can continuously control radial and axial injection areas and thereby simultaneously change corresponding mass flow rates of fuel and oxidizer, where the radial and axial flows encounter to form a spray cone and then develop to subsequent spray atomization. For each injection element uniformly distributed along the circumferential direction of the pintle, it adopts either film-film or jet-film collision. For the film-film collision [9,10], two films emitting respectively from radial and axial directions collide to form a hollow conical liquid film. The subsequent development of surface capillary waves and film fragmentation results in a spray distributed away from the axis. For the jet-film collision [11–13], the radial jet collides with the axial film to create a spray distributed in the vicinity of the axis and the radial direction. Compared with the film-film injection element, the jet-film injection element is frequently used in the practical pintle injector for its more optimized spray characteristics [5] owing to the synergetic jet- and film-breakup mechanisms.

Many parametric studies were conducted on the spray atomization and subsequent combustions of the pintle injector, for example, the influences of geometric or flow parameters on the spray angle [10–12,14,15], the process of film fragmentation, atomization, and mixing characteristics between fuel and oxidizer [16–18], and the spray combustion stabilities [17,19,20]. Apart from the spray atomization and combustion, the physical and mathematical models for the evaporation, ignition, and combustion in poly-dispersed non-uniform fuel sprays have been studied in previous studies. For example, Betelin et al. [21] numerically studied the single droplet evaporation in a streaming flow and the modeling of evaporating and combustion for fuel sprays. Smirnov et al. [22–24] studied the ignition and combustion onset of a heterogeneous mixture with droplet non-uniformity in space and size

* Corresponding author.
E-mail address: yuelj@imech.ac.cn (L. Yue).

https://doi.org/10.1016/j.actaastro.2023.02.006
Received 27 December 2022; Received in revised form 3 February 2023; Accepted 5 February 2023
Available online 10 February 2023

Nomenclature

Physical quantities

D	Droplet diameter
h	Film thickness
$\dot{m}_j, \dot{m}_f$	Mass flow rates for liquid jet and film, respectively
t	Physical time
t_{osc}	Characteristic oscillation time, $t_{osc} = (\rho D^3/\sigma)^{1/2}$
v_j, v_f	Injection velocities for liquid jet and film, respectively
w	Film width
μ	Liquid dynamic viscosity
ρ	Liquid density
θ	Spray angle of jet-film collision element
σ	Surface tension coefficient

Non-dimensional and normalized variables

Oh	Ohnesorge number, $Oh = \mu/\sqrt{\rho D\sigma}$
T	Non-dimensional time, $T = t/t_{osc}$
We_j	Weber number, $We_j = \rho D v_j^2/\sigma$, for liquid jet
We_f	Weber number, $We_f = \rho h v_f^2/\sigma$, for liquid film

Abbreviations

BF	Blockage factor
LMR	Local momentum ratio
PDF	Probability Density Function
SMD	Sauter Mean Diameter
TMR:	Total momentum ratio
VOF	Volume-of-Fluid method

distribution. It consolidated our understanding that the effects of non-uniformity of droplet size and spatial distribution are the key factors for the fuel droplet atomization, evaporation, ignition delay and mild initiation of detonation, and subsequent combustion process.

For the spray characteristics of moveable pintle injectors at different throttling levels, a few studies adopted variable geometric parameters [13–15,25] to change the opening outlet area and thereby the mass flow rate. Lee et al. [13] experimentally studied different throttling levels of the radial flow and obtained an optimal throttleable pintle injector with high atomization efficiency from the aspects of spray angle, spray uniformity, and droplet size distribution. Heo et al. [15] experimentally found that adopting a grooved pintle tip to change the structure of the radial flow can improve the spray characteristics and reduce the great changes of spray characteristics with varying throttling levels, which is advantageous from the perspective of design simplicity. Radhakrishnan et al. [25] studied the mixing performance at a different opening distance of the pintle injector and found that the low mixing quality at a small opening distance can be improved by increasing the mass flow rate or the opening distance of the pintle. However, it is noted that the above studies concerned only the change of outlet area of the radial flow but not the corresponding change of the axial annular film flow. For the situation with approximately fixed injection pressure or velocity, the mass flow rate is merely related to the injection area, and the radial and axial flow areas should be changed simultaneously at different throttling levels to ensure the optimized fuel-oxidizer mass ratio. In that situation, two prominent disadvantages of the jet-film injection element on the spray characteristics appear. First, the axial film thickness is generally very thin when compared to the radial jet diameter, and it is extremely difficult to further reduce the film thickness at a small mass flow rate with a high accuracy. Second, the thinner film at a small mass flow rate can weaken the local jet-film collision and increase the spray angle, leading to poor spray characteristics varying greatly with the changing of throttling levels.

To solve the possibly poor spray characteristics of pintle injectors with varying mass flow conditions, we proposed a new design concept that adopts a traditional jet-film injection element at a large mass flow rate and a modified jet-jet injection element at a small mass flow rate to ensure the optimized spray angle and atomization are insensitive to the change of injection areas in the entire engine throttling range. The jet-jet injection element is achieved by blocking the axial annular flow to form various orifices that one-by-one correspond to the radial injection orifices. In that situation, the original film thickness is fixed, and the axial flow area is merely controlled by the film width along the circumferential direction. The present paper intends to consolidate the understanding of the jet-film injection element in the pintle injector and computationally verify our design concept. It is worth mentioning that the flow field of a real pintle injector shows periodic characteristics

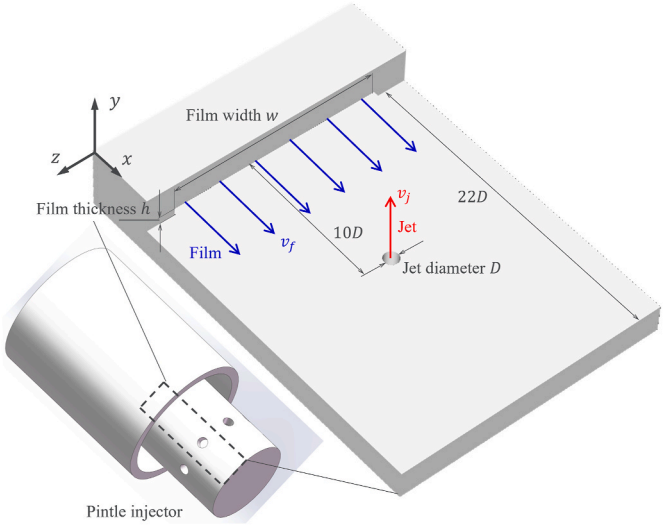

Fig. 1. Schematic of a pintle injector and its jet-film collision element.

along the circumferential direction and each injection orifice can be treated as an independent jet-film collision element. Thus, to reduce a large amount of computational cost, the present study mainly focuses on the simplified model of the collision between a jet and a planar film, as the schematic shown in Fig. 1.

To quickly prescreen designs of pintle injectors, it is often sufficient to conduct cold flow tests because good atomization characteristics generally produce efficient combustion. A very common approach to evaluating the spray characteristics is using the Sauter Mean Diameter (SMD) [13,26–29], which shows the mean characteristic diameter at a spatial position during a period of time for a stable spray. However, a locally small SMD of sprays does not guarantee good combustion because droplet clustering characterizing the interaction between neighboring droplets is not reflected in SMD. Droplet clustering in sprays influences the flame propagation speed and the local combustion mode between the single droplet combustion and the group droplet combustion [30–32]. Srikrishna [33–35] proposed an approach to analyzing the droplet clustering from the topological aspects by using the Voronoi tessellation, in which a defined group combustion number was evaluated for each droplet cluster showing multi-scale droplet clustering and multi-mode combustion of the clusters during the spray burning process.

The present paper is organized as follows. The numerical method and validation are presented in Sec. II, followed by the analysis of spray characteristics of a representative jet-film collision element by using

SMD and Voronoi tessellation in Sec. III, and the effects of film thickness and width on the spray characterizations with varying mass flow rate conditions in Sec. IV, respectively.

2. Computational methodology

2.1. Problem description

Three controlling design parameters were considered in the study, namely the jet diameter D, the thickness h, and the width w of axial film, which influences the spray characteristics of a jet-film injection element.

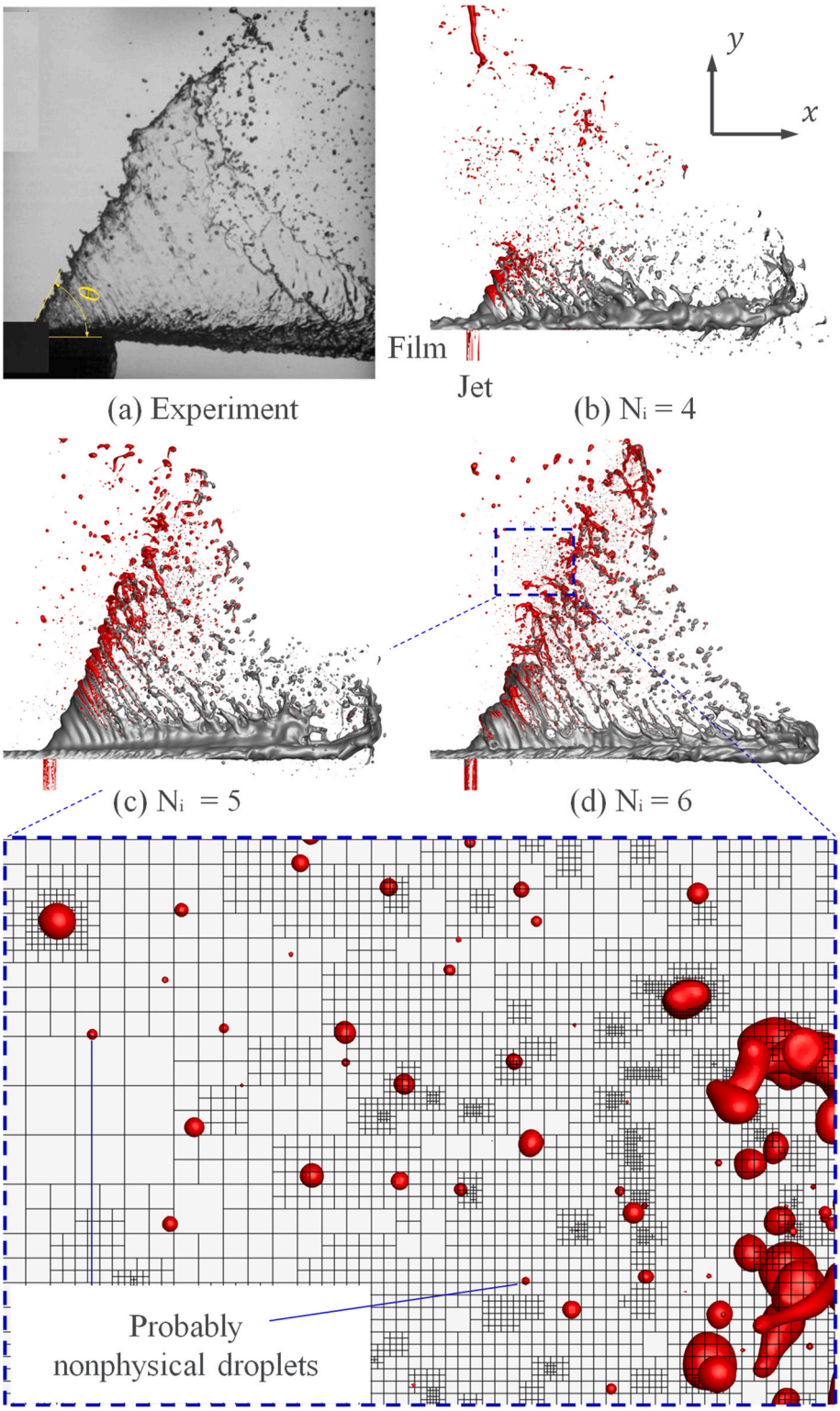

Fig. 2. Comparison of spray angle and breakup characteristics upon the jet-film collision between (a) Cheng's experiment [11] and (b–d) present simulations at $We_f = 370$ and $We_j = 543$ with different mesh refinement levels N_i, in which a close-up of probably nonphysical droplets is shown for $N_i = 6$.

The solid model of the jet-film collision element, as shown in Fig. 1, has a length of 22D and a skip distance between the outlet of the axial film and the radial jet of 10D. The cuboid computational domain has a length of 100D and a width and height of 30D respectively. All boundaries except the inlet are specified as free outflow boundary conditions, and the solid model is set as the immersed non-slip wall boundary.

For the typical film-film injection element, Cheng et al. [12] proposed the relation between the spray angle θ and the total momentum ratio (TMR) as $\cos\theta = (1+\mathrm{TMR})^{-1}$; whereas for the jet-film injection element, Cheng et al. [11] found that using the local momentum ratio (LMR) to replace TMR so as the relation of spray angle with momentum ratio is still valid. The results showed that the spray angle increases with LMR and generally had a good agreement between the experiment and theoretical model except for some underestimations of theoretical spray angle for the multiple rows of radial holes or the square holes with large length-width ratios.

For each jet-film collision element, the local momentum ratio is defined as

$$\mathrm{LMR} = \frac{\mathrm{TMR}}{\mathrm{BF}} = \frac{\dot{m}_j v_j}{\dot{m}_f v_f}\frac{w}{D} \tag{1}$$

where $\mathrm{TMR} = \dot{m}_j v_j / \dot{m}_f v_f$ is the total momentum ratio, $\dot{m}_j$, v_j and $\dot{m}_f$, v_f the mass flow rate and injection velocity for the radial jet and axial film flow, respectively, and $\mathrm{BF} = D/w$ the blockage factor. For the traditional jet-film pintle injector as decreasing the mass flow rate to different throttleable levels, the decrease of axial and radial mass flow rates is controlled by respectively reducing the film thickness h and the jet diameter D with the mass ratio $\dot{m}_j/\dot{m}_f$ and injection velocities v_j and v_f being fixed. Thus, as decreasing mass flow rates, TMR is unchanged but LMR increases owing to the decreased BF (w is fixed), which causes an increase of spray angle that deviated from the optimal value of about 45°, and subsequent possibly poor spray characteristics. This motivates us to propose the new design in the present study by simultaneously changing jet diameter D and film width w rather than film thickness h as varying the mass flow rate so that LMR is approximately insensitive to the variation of different throttleable levels.

The other non-dimensional parameters are given as follows. The collision Weber numbers of jet and film are $We_j = \rho D v_j^2/\sigma$ and $We_f = \rho h v_f^2/\sigma$ respectively (ρ is the liquid density and σ the surface tension coefficient), measures the relative importance of the jet or film impact energy compared with its surface energy. The Ohnesorge number, $Oh = \mu/\sqrt{\rho D\sigma}$ (where μ is the dynamic viscosity of the liquid), measures the relative importance of the liquid viscous stress compared with the capillary pressure. The Reynolds number represents the relative effect of inertia force versus viscous force, which can be calculated by Oh and We as $Re = \sqrt{We}/Oh$. For the liquid water jet with a characteristic diameter of 1000 μm, the dimensionless time is defined as $T = t/t_{\mathrm{osc}}$ and $t_{\mathrm{osc}} = (\rho D^3/\sigma)^{1/2} = 3.7$ ms.

2.2. Computational methodology

The three-dimensional (3D) continuity and incompressible Navier-Stokes equations,

$$\nabla\cdot\boldsymbol{u} = 0 \tag{2}$$

$$\rho(\partial\boldsymbol{u}/\partial t + \boldsymbol{u}\cdot\nabla\boldsymbol{u}) = -\nabla p + \nabla\cdot(2\mu\boldsymbol{D}) + \sigma\kappa\boldsymbol{n}\delta_s \tag{3}$$

are solved by using the classic fractional-step projection method, where $\boldsymbol{u}$ is the velocity vector, ρ the density, p the pressure, μ the dynamic viscosity, and $\boldsymbol{D}$ the strain rate tensor defined as $D_{ij} = (\partial_j u_i + \partial_i u_j)/2$. In the surface tension term $\sigma\kappa\boldsymbol{n}\delta_s$, δ_s is a Dirac delta function, σ the surface tension coefficient, κ the local curvature, and the unit vector $\boldsymbol{n}$ normal to the local interface.

The present study adopts the Volume-of-Fluid (VOF) method. To solve both the gas and liquid phases, the density and viscosity are constructed by the volume fraction as $\rho = c\rho_l + (1-c)\rho_g$ and $\mu = c\mu_l + (1-c)\mu_g$, in which the subscripts l and g denote the liquid and gas phases, respectively. The volume fraction c satisfies the advection equation

$$\partial c/\partial t + \nabla\cdot(c\boldsymbol{u}) = 0 \tag{4}$$

with $c = 1$ for the liquid phase, $c = 0$ for the gas phase, and $0 < c < 1$ for the gas-liquid interface.

Two major challenges of spray simulation are the accurate prediction of the primary breakup of liquid jet or film and the extremely fine mesh resolution for a large number of dispersed droplets and secondary breakup. Generally, the direct numerical simulation (DNS) of sprays [36,37] with accurate interface tracking methods [38–40] can provide more details with appropriate mesh resolution to certain physical problems. For example, Salvador et al. [36] analyzed the effects of turbulent inflow conditions on the primary breakup of a liquid jet by DNS with approximately 66 million cells and a minimum cell of 2.34 μm. Shinjo and Umemura [37] performed a DNS of the primary breakup of a liquid jet with a total mesh number of about 6 billion and a minimum mesh grid of 0.35 μm. To reduce the substantial computational cost of DNS of sprays, the coupled Eulerian-Lagrangian approach [41–43] was proposed to combine the Eulerian method for the primary breakup of liquid jet or sheet and the Lagrangian model for the dispersed droplet dynamics, where all small droplets with diameters that smaller than the reference value would be transformed into Lagrangian particles. Zaripov et al. [44] simulated the dilute gas-particle flow around a cylinder and liquid droplets in a gasoline fuel spray by using the code ANSYS Fluent with Discrete Phase Model (DPM), and produced good qualitative numerical results to experimental observations. Li and Soteriou [45] compared three grid configurations for the direct numerical simulation of a liquid jet in gas crossflow with a total mesh number of about 503 million for the uniform grid, 7.1 million for the adaptive mesh refinement grid, and 5.5 million for adaptive mesh refinement with additional coarsening via the introduction of Lagrangian droplets.

In the present study, the direct numerical simulation, i.e. Eulerian approach, with the VOF method implemented in the open source code, Gerris [40,46,47], is adopted to analyze the spray characteristics of the jet-film collision element. Gerris features the 3D octree adaptive mesh refinement, the geometrical VOF interface reconstruction, and continuum surface force with height function curvature estimation, which has been demonstrated to be competent for high-fidelity simulation of the breakup of liquid jets [48,49] or films and subsequent spray atomization [28,29,42,50–52].

2.3. Numerical validation

To justify the computational approach discussed above, the experimental validation and grid-independence analysis for the case of $We_f = 370$ and $We_j = 543$ from Cheng et al. [11] are shown in Figs. 2 and 3. To improve computational efficiency, the entire computational domain is divided into three physical zones, namely the gas, the liquid, and the gas-liquid interface zones, and different mesh refinement levels (N_g, N_l, N_i) are used in these zones, respectively. Generally, N_i for the gas-liquid interface zone plays a dominant role in capturing jet or film breakup characteristics, and N_g for the gas zone and N_l for the liquid zone are one level smaller than N_i to reduce the total number of meshes. In the present study, $N_g = N_l = 3$ are fixed and three different levels, $N_i = 4, 5, 6$, corresponding to the minimum dimensional cell size of 62.5 μm, 31.2 μm, and 15.6 μm, respectively, are analyzed by comparing the simulation results and Cheng's experiment [11] of the collision between a jet and a film, in which red and gray contours denote the liquid mass of jet and film respectively.

Fig. 2 shows the comparison of spray angle and jet-film breakup characteristics between experiment and simulation results for different mesh refinement levels. It is seen that the spray angles around the jet-

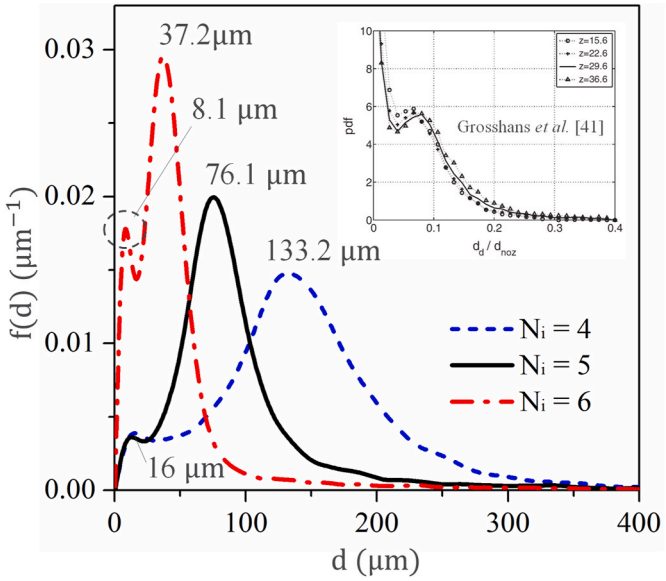

Fig. 3. Probability Density Function (PDF) of the diameter of discrete droplets for the simulation results in Fig. 2 with different mesh refinement levels N_i.

film collision position for three different levels are approximately the same, which is also consistent with the experimental observation of about 60° shown in Fig. 2(a). The film formation upon the jet-film collision is insufficient for the coarse mesh with $N_i = 4$, as shown in Fig. 2(b), leading to the numerically suppressed jet fragmentation and a low number density of atomized droplets away from the jet-film collision point. For a refined mesh with $N_i = 5$ in Fig. 2(c), the numerical results of jet-film collision present a typical cone-shape structure and qualitatively agree with the experimental images. As further refining mesh to $N_i = 6$ in Fig. 2(d), the spray shape and breakup characteristics are approximately the same as those for $N_i = 5$.

To further verify the mesh refinement effects on the sprays quantitatively, the comparison of the Probability Density Function (PDF) of dispersed droplet diameter is shown in Fig. 3. All fluid parcels with discrete spatial distribution of the VOF volume fraction are identified as the dispersed droplets by using a built-in function in Gerris, in which the effective droplet diameter is evaluated by the volume-to-surface characteristic length for each liquid parcel. The results show that PDF is an approximately Poisson distribution for all the cases, and the peak value of PDF increases and shifts towards a smaller droplet diameter as increasing the mesh refinement level. The droplet diameter at each PDF peak for $N_i = 4, 5, 6$ are 133.2 μm, 76.1 μm, and 37.2μm respectively, which is approximate twice the minimum mesh size of about 62.5 μm, 31.2 μm, and 15.6 μm. It is noted that a smaller peak of PDF for $N_i = 6$ is observed with the droplet diameter of 8.1 μm which is even smaller than the minimum mesh size of 15.6 μm. This is because some probably nonphysical droplets are formed, as the closeup of dispersed droplets for $N_i = 6$ shown in Fig. 2. These numerical droplets are not supposed to occur for the pure Eulerian approach based on the VOF method since no additional strategy of dispersed droplets transformed into the Lagrangian mass has been implemented in the present study. Similar numerical results of PDF were also reported by Grosshans et al. [41,53], as the embedded figure shown in Fig. 3. The coupled Eulerian-Lagrangian approach was proposed [41,43] to remedy the inherent drawbacks of a full VOF simulation in dealing with the primary breakup of jet or film: strong grid dependence of PDF and substantial computational costs for the secondary breakup of sprays. The previous studies [41,53] suggest that the VOF simulation results are still reliable if we ignored the peculiar peak of the PDF in the range of small droplet sizes because the very small droplets that badly resolved in the VOF approach are insignificant to the total liquid mass and the related error is therefore negligible.

In addition, the accumulation error for the used open-source code, Gerris, is analyzed. Referring to the error analysis method [54,55], the relative error of integration in one dimensional case is defined as $S_i = (\Delta L/L_i)^{k+1}$, where ΔL is the smallest cell size, L_i the domain size in one dimensional, and k the order of accuracy of numerical scheme. For the adaptive mesh refinement in the present simulation, the smallest cell occurs on the gas-liquid interface with the size of $1/2^{N_i}$, and then the relative error can be expressed as $S_i = (1/2^{N_i}L_i)^{k+1}$. For the three-dimensional simulation, the total interaction error is $S_{err} = \sum_{i=1}^{3} S_i$, where the presumed error value is generally less than 5%. The allowable value of total error S^{max} after the solution satisfies $S_{err} \bullet \sqrt{n} \le S^{max}$, where n is the number of time steps in the integration. The maximal allowable number of time steps is determined as $n_{max} = (S^{max}/S_{err})^2$. The time step ratio $R_S = n_{max}/n$ characterizes the reliability of results, indicating that the higher R_S leads to lower error and R_S closing to unity denotes the maximal allowable error. Consequently, the accumulation error analysis with different mesh resolution is present in Table 1. The results show that the accumulation errors decrease as increasing the mesh refinement and scheme accuracy, and all simulations demonstrate high reliability of the present code.

In the present study, the intermediate mesh refinement level $N_i = 5$ was used for all simulation cases based on the following considerations. First, the spray cone and breakup characteristics are approximately unchanged with further increasing N_i and qualitatively agree with the experiment; Second, a coarse mesh improves the computational efficiency and reduces the possibility of nonphysical droplets generated on a refiner mesh; Third, the droplet diameter at the PDF peak for $N_i = 5$ is the order of $O(100)$ μm, which is consistent with the droplet diameter measurement in previous experiments [48] under the injection velocity condition of a jet in the order of $O(10)$m/s. A typical simulation run with the mesh refinement level (3,3,5) results in about 4.0×10^6 grid points in the entire domain, taking about 165 h of real-time to simulate up to T = 1.5 on one AMD EPYC 7452 processor with 64 cores.

3. Spray characterizations of jet-film collision

3.1. Phenomenal description of the jet-film collision

A representative case of jet-film collision at $We_f = 742$ and $We_j = 2119$ is analyzed in this section, corresponding to the dimensional injection velocity of $v_j = 12.26$m/s and $v_f = 10.21$m/s and dimensional mass flow rate of $m_j = 10.2$g/s and $m_f = 81.9$g/s, respectively, which is in the range of injection velocity of a real rocket engine. The simulated liquid jet and film are water, with the jet diameter $D = 1$ mm, film thickness $h = 0.52$ mm, and film width $w = 15$ mm.

Fig. 4 compares the experimental image and simulation results of the

Table 1
Accumulation error analysis.

Allowable error (%)	Mesh resolution (N_g, N_l,N_i)	Physical time simulated (μs)	Number of time steps (n)	Accumulated error (S_{err})	Allowable number of time steps (n_{max})	Reliability ($R_s = n_{max}/n$)
5	(3, 3, 4)	5.6	4001	1.83286E-08	7E+12	1.86E+09
5	(3, 3, 5)	5.6	4236	2.29108E-09	5E+14	1.124E+11
5	(3, 3, 6)	5.6	13616	2.86385E-10	3E+16	2.239E+12

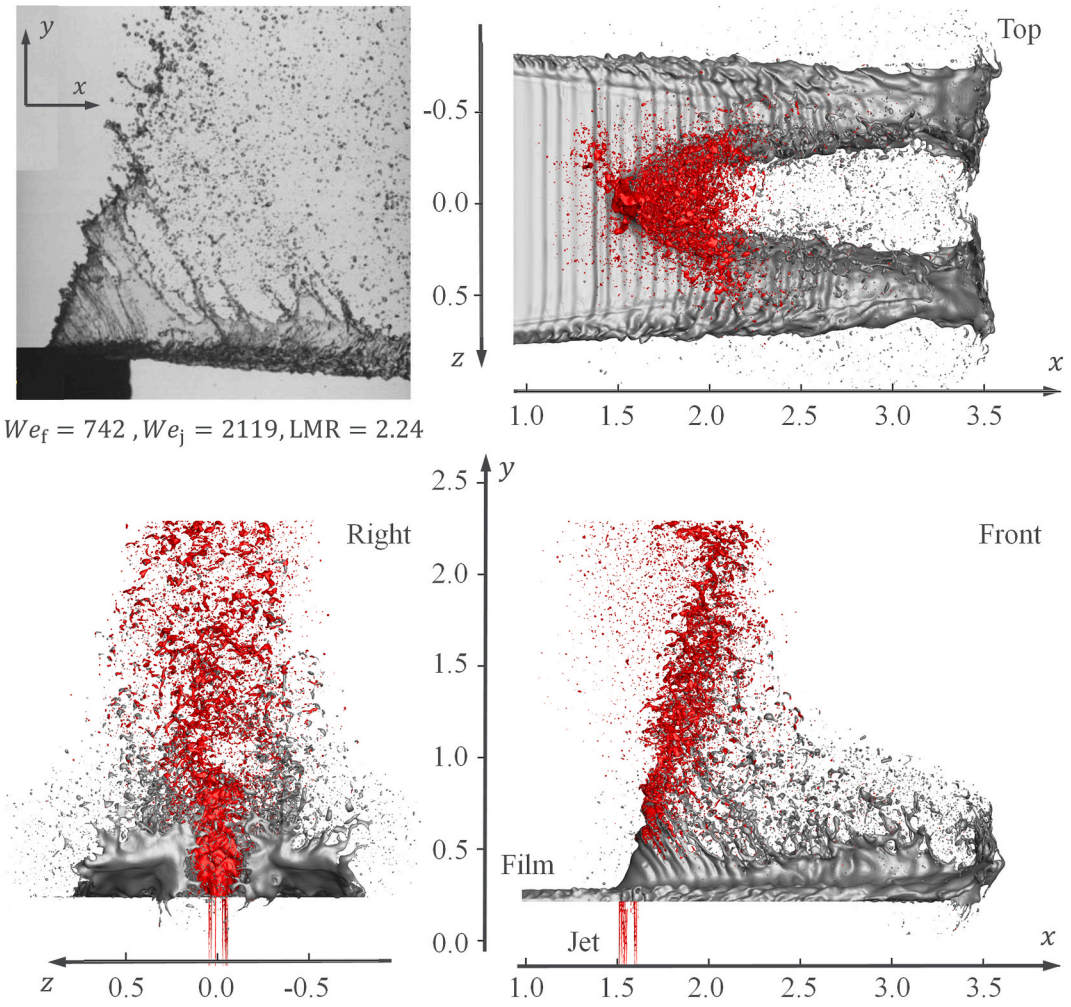

Fig. 4. Experimental image (extract from Cheng's experiment [11]) and simulation results of spray contour from three different views for a representative jet-film collision at $We_f = 742$ and $We_j = 2119$.

contour in three different views. Again, the spray angle shown in the front view is consistent with the experimental observation with a value of about 70°, which is larger than that shown in Fig. 2(a) owing to the increased LMR. The typical cone-shaped structure of the jet-film collision also qualitatively agrees with the experimental images. The jet marked by red dyed function penetrates through the film marked by gray, leading to the jet liquid mass mainly spreading over in the *y*-direction (equivalent to the radial direction in real pintle injectors) and film liquid mass is mainly distributed around the *x*-axis (equivalent to the axial direction in real pintle injectors). Two more views from the top and right sights provide some additional information about sprays that cannot be seen in the experiment. The dense sprays mainly occur around

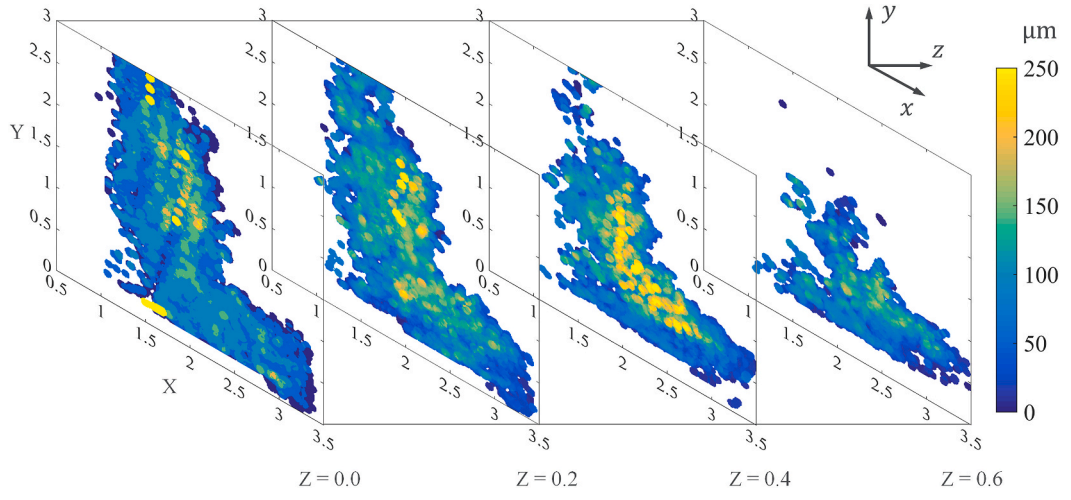

Fig. 5. Contour of Sauter Mean Diameter (SMD) at different slices of $z = 0.0 \sim 0.6$ for the representative case shown in Fig. 4.

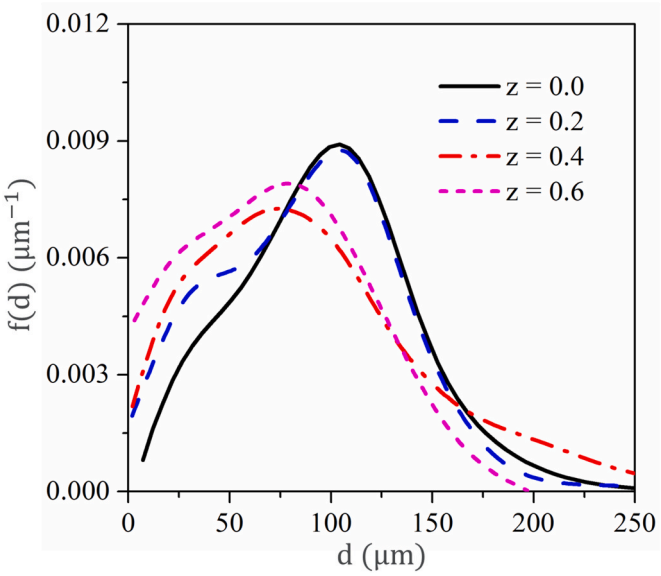

Fig. 6. Probability density function (PDF) of Sauter mean diameter (SMD) at different $z = 0.0 \sim 0.6$ for the representative case in Fig. 4.

the jet and the jet-film interaction region, which is caused by the synergetic roles of jet and film breakup mechanisms. It is also seen the dilute sprays after the jet in the *x*-direction and other film regions without impacting the jet because the film width is sufficiently larger than the jet diameter. In addition, it shows non-uniform spray characteristics along the *z*-direction (equivalent to the circumferential direction in real pintle injectors). To clearly illustrate the spatial characteristics of sprays, the coordinate is shown for each figure and all coordinate values at *x*-, *y*-, and *z*-directions have been scaled with a factor of 0.1.

The Kelvin-Helholz instability is likely occurring around the gas-liquid interface of jet or film due to the different velocities for the gas and liquid phases. Physically, the jet or film breakup can be divided into few stages. In the early stage, the Kelvin-Helholz instability [56] probably develops on the jet or film interface accompanied by the developed capillary waves owing to the shear velocity between gas and liquid phases; in the middle stage, the R-T instability [57] may drive the interface with enhanced capillary waves into multiple finger structures owing to the magnified perturbation where there is a density jump across the liquid-gas interface; and in the late stage, the gas-liquid interface starts to breakup into smaller droplets that caused by the Plateau-Rayleigh instability [58].

3.2. Sauter Mean Diameter

Apart from the qualitative description, the statistical distribution of

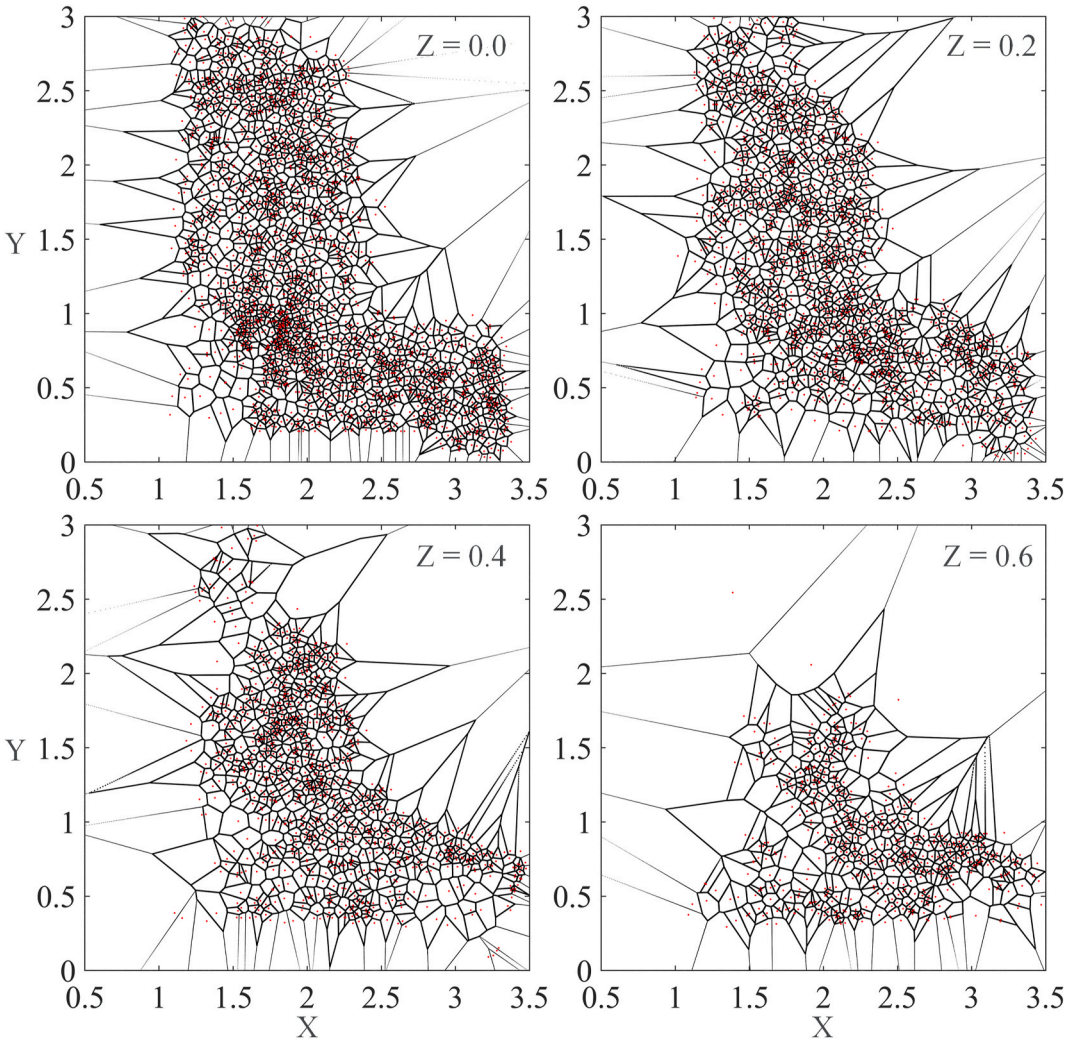

Fig. 7. Voronoi diagram of all dispersed droplets at different $z = 0.0 \sim 0.6$ for the representative case in Fig. 4.

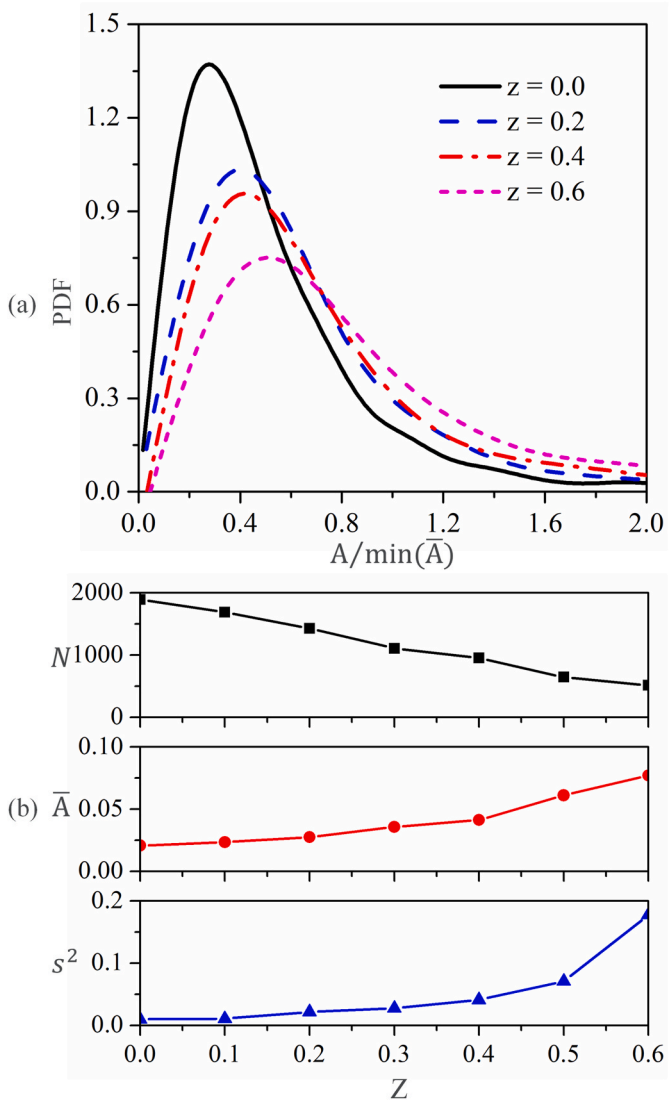

Fig. 8. Comparison of (a) probability density function (PDF) of Voronoi volumes and (b) the discrete droplet number, mean Voronoi volume, and square deviation of Voronoi volumes at different $z = 0.0 \sim 0.6$ for the representative case in Fig. 4.

atomized droplet size can be quantified by characteristic diameter [26]. The discrete form of characteristic diameter is defined as

$$D_{pq} = \frac{1}{t}\sum_{\Delta t=1}^{t}\left[\frac{\sum_{i=1}^{\infty} n_i D_i^{\,p}}{\sum_{j=1}^{\infty} n_j D_j^{\,q}}\right]^{1/(p-q)} \tag{5}$$

where p and q are positive integers, n the number of droplets with a diameter of D, and t the number of total discrete sampling time. In general, the Sauter Mean Diameter (SMD), D_{32}, is the most representative one that measures the volume-to-surface ratio of a finite fluid parcel. The quantitative analysis of the contour of SMD at different z coordinates is presented in Fig. 5, in which the statistical droplet information for each slice is analyzed at a certain z coordinate with a finite thickness equaling to the characteristic length. The contour results show that the area occupied by large SMD (or larger than 250μm) increases from $z = 0.0$ to the maximum at $z = 0.4$ and then decreases to a small value at $z = 0.6$, showing a non-monotonic variation along the z-direction. Whereas the area of nonzero SMD is largest at $z = 0.0$ and monotonically decreases with z because the jet-film impact point is located at $z = 0.0$ and their interaction is increasingly weakened as being away from the impact point, as shown in Fig. 5.

Fig. 6 further shows the PDF of SMD at different z coordinates. It is seen that both the droplet size and PDF value at the peak point of SMD decrease as increasing z, which indicates that the strong jet-film impact at $z = 0.0$ generates a large number of atomized droplets spreading over a wide region but the droplet size is relatively large, whereas the weak jet-film impact away from $z = 0.0$ causes smaller droplets but only distributed in a narrow region, which is consistent with the contour of SMD shown in Fig. 5. For the representative slice at $z = 0.4$, as the curve shown in Fig. 6, the droplet size at the peak of SMD is smaller than other slices, however, large SMDs are also observed in the range between 200μm to 250μm, showing an extreme non-uniform distribution of SMD. Compared with the axisymmetric film-film collision as discussed in the introduction, the jet-film collision shows lots of local characteristics of sprays that merit further analysis. The best spray characteristics tend to simultaneously have a smaller SMD but also a uniform distribution of dispersed droplets. This motivates us to analyze the atomized droplets by using the Voronoi tessellation in the following.

3.3. Dispersed droplet distribution by Voronoi tessellation

To analyze the spatial distribution of dispersed droplets, Voronoi tessellation [33,34,59,60] has been used to identify the influence region for each dispersed droplet. As the 2D example at $z = 0.0$ shown in Fig. 7, Voronoi tessellation divides the entire space into many subspaces around droplets and guarantees every point in a subspace is closer to its corresponding droplet coordinate than other droplets. As a result, the points on a boundary between two subspaces have the same distance to the droplets belonging to the subspaces. Voronoi tessellation can be mathematically described as that, for each droplet j occupying the coordinate $\boldsymbol{x}_j$, its influence region $R(j)$ is defined as

$$R(j) = \left\{\boldsymbol{x} \in \mathbb{R}^n \middle| d^0(\boldsymbol{x}, \boldsymbol{x}_j) \le d^0(\boldsymbol{x}, \boldsymbol{x}_k), \text{for all } k \ne j\right\} \tag{6}$$

where $\boldsymbol{x}$ is the coordinate for a droplet in the Euclidean space $\mathbb{R}^n$ (n is the dimension), and d^0 is the natural Euclidean metric (distance function).

Fig. 7 shows the Voronoi diagram at different z coordinates. It is seen the dense spray with large number density of dispersed droplets or small Voronoi volumes and diluted spray with small number density of dispersed droplets or large Voronoi volumes. The dense spray mainly occurs close to $z = 0.0$ and is diluted as varying the z coordinate because the jet-film collision around $z = 0.0$ causes a large number of dispersed droplets. As shown in Fig. 8(a), as increasing the z coordinate, the PDF value decreases but the normalized volume at the peak of PDF increases, indicating the majority of Voronoi cells with small Voronoi volumes are distributed in the vicinity of the jet-film collision region, namely close to $z = 0.0$, in which min $(\bar{A})$ is the minimum of all Voronoi volumes. Thereby, the number of droplets and mean Voronoi volume respectively decrease and increase as being away from the impact plane $z = 0.0$, as shown in Fig. 8(b). To quantitatively characterize the uniformity of dispersed droplets, the square deviation of Voronoi volumes is defined as $s^2 = \sum_i^{\infty}(A_i - \bar{A}_i)/N$ and shown in Fig. 8(b). For locations being away from impact point, although the SMD shown in Fig. 6 is small, the square deviation s^2 is large, indicating it is possibly unreasonable to evaluate the spray characteristics by only one indicator of either SMD or square deviation.

Fig. 9 compares the SMD contour and Voronoi cells at $z = 0.0$ and $z = 0.4$. The results show that there is no prominent correlation between SMD and Voronoi volumes, for example, as the white squares 1 and 2 shown in Fig. 9(a), the approximate SMD distribution leads to dense spray (small Voronoi volumes) in square 1 and dilute spray (large Voronoi volumes) in square 2; similarly, for the approximately Voronoi cells shown in Fig. 9(a) and (b), the SMD at $z = 0.4$ is prominently larger than that at $z = 0.0$. It is inferred that both the Voronoi diagram and the SMD contour are significant to evaluate the spray characteristics because they reflect two different aspects of the spray. The SMD contour reflects the

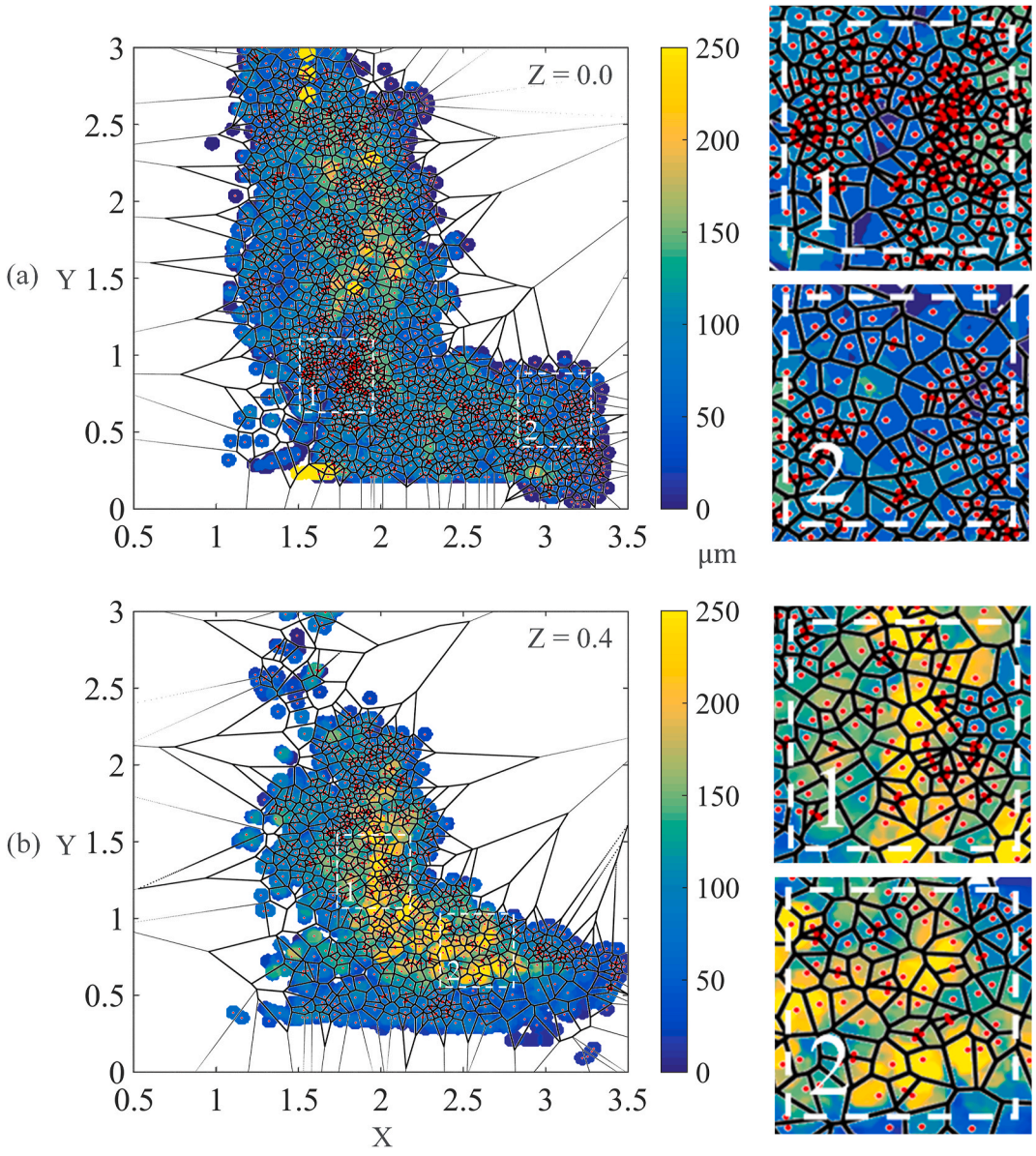

Fig. 9. Spatial distribution of SMD contour and Voronoi diagram at (a) $z = 0.0$ and (b) $z = 0.4$, respectively.

time average of discrete droplets at a certain spatial location, whereas the Voronoi cells reflect the local characteristics of discrete droplet distribution at a certain time. The droplet clustering effects characterized by Voronoi tessellation in sprays influence the local combustion mode of spray combustion. The coupling effects of SMD and Voronoi distribution can benefit a complete sub-grid model for group combustion [33–35] in spray combustion, which provides some new understanding and theoretical references of the spray combustion and merits studies in the future.

4. Effects of film thickness and width

In the present study, the variation of mass flow rates m_j and m_f are achieved by varying injection areas, namely jet diameter D, film thickness h, and width w, with approximately fixed injection velocities for the convenience of injection pressure drop control of a real throttleable pintle injector. This section focuses on numerically verifying the design idea as discussed in the introduction that adopting a traditional jet-film injection element at a large mass flow rate and a modified jet-jet injection element at a small mass flow rate to adjust the local momentum ratio and improve the spray characteristics during the entire throttleable range of mass flow rate.

4.1. Effects of film thickness

Fig. 10 shows the SMD contour and Voronoi diagram for different film thickness h but fixed film width w. As reducing mass flow rate by decreasing the film thickness, the 100%, 50%, and 25% throttleable levels in Fig. 10(a–c) respectively correspond to the local momentum ratio LMR of 2.24, 3.17, and 4.48, resulting in an increase of the spray angle from about 70° in Fig. 10(a) to approximately 90° in Fig. 10(c) and significantly deviated from the optimal spray angle. Although a thinner film in Fig. 10(c) is more easily to break up for itself, the effective impact inertia upon the jet-film collision is weakened, leading to the impact inertia distributed either along the axial direction for the film or the radial direction for the jet and thereby an extremely nonuniform distribution of dispersed droplets. This is because the radial jet is nearly uninfluenced by the axial film, where the breakup of the jet is merely controlled by jet instability instead of the synergetic mechanisms of jet-film interaction, and thereby the jet breakup is weakened with a large

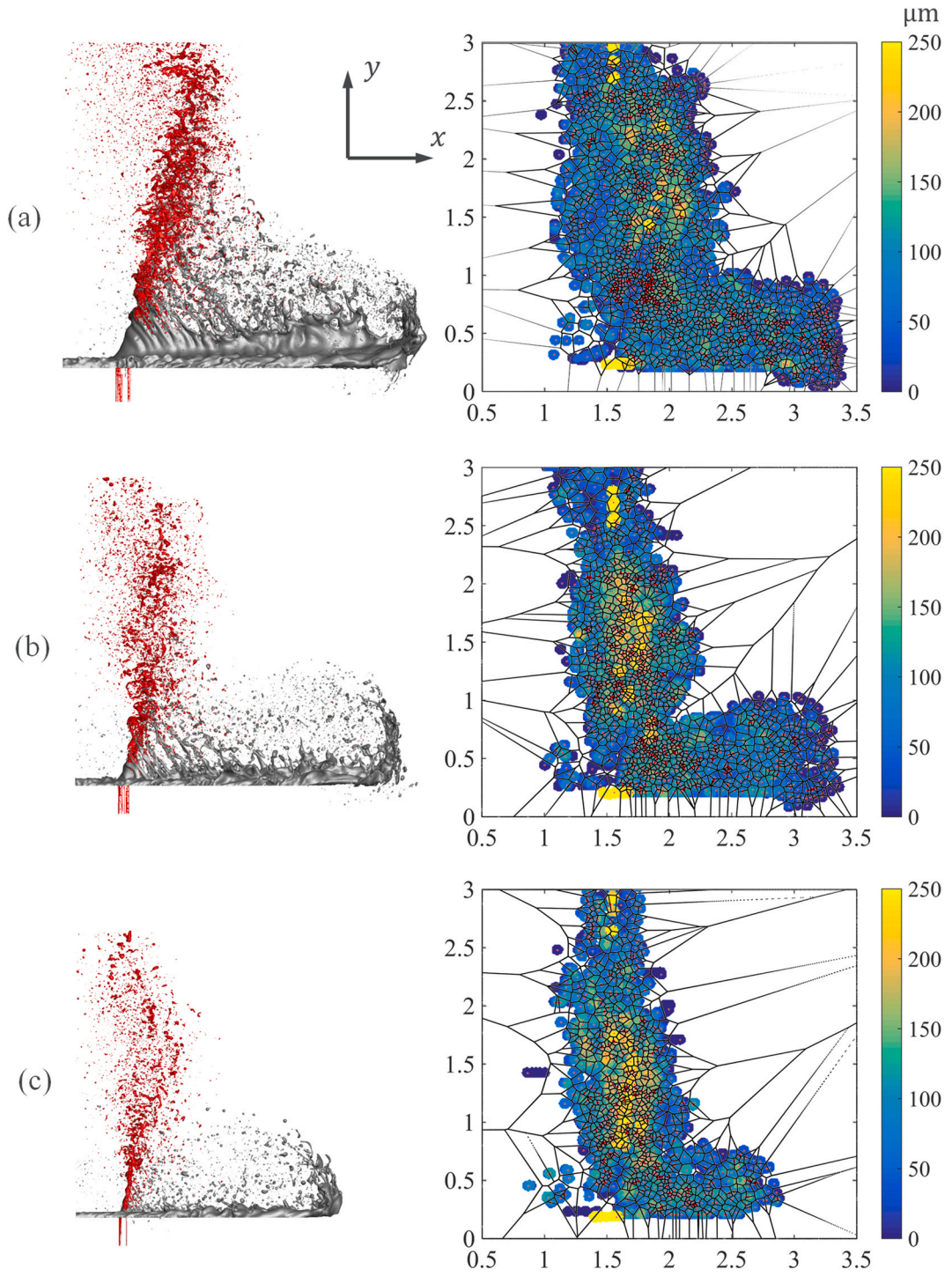

Fig. 10. Comparison of spray characteristics and SMD contour and Voronoi diagram at $z = 0.0$ for different film thicknesses. (a) $h = 0.52$ mm at 100% throttleable level, (b) $h = 0.26$ mm at 50% throttleable level, and (c) $h = 0.13$ mm at 25% throttleable level, with fixed $w = 15$ mm as decreasing the mass flow rate.

SMD distribution as shown in Fig. 10(c). In addition, the region area of nonzero SMD contour is reduced, and the region with relatively large SMD is enlarged decreasing the mass flow rate.

To further characterize the spatial characteristics of sprays with varying mass flow rates, Fig. 11 quantitatively shows the PDF of discrete droplets diameter, PDF of Voronoi volumes, and the number, mean Voronoi volume, and square deviation for different film thicknesses. As decreasing the film thickness h, both the PDF value and the droplet diameter at the peak of PDF in Fig. 11(a) decrease slightly, indicating a thinner film favors smaller droplets but the number of small droplets is also reduced. The decrease of film thickness h results in an increased PDF value but a decreased Voronoi volumes at the peak of PDF for $h = 0.13$ mm, as shown in Fig. 11(b), which indicates a thinner film tends to generate some local clustering droplets with a smaller Voronoi volume (in other words the neighboring droplets are closer to each other), however, the droplet clustering is locally and the global uniformity of droplet distribution is reduced, as the increased square deviation shown in Fig. 11(c). A conclusion can be obtained that the spray characteristics of jet-film collision become worse by decreasing the film thickness for different mass flow rate conditions owing to the increased spray angle

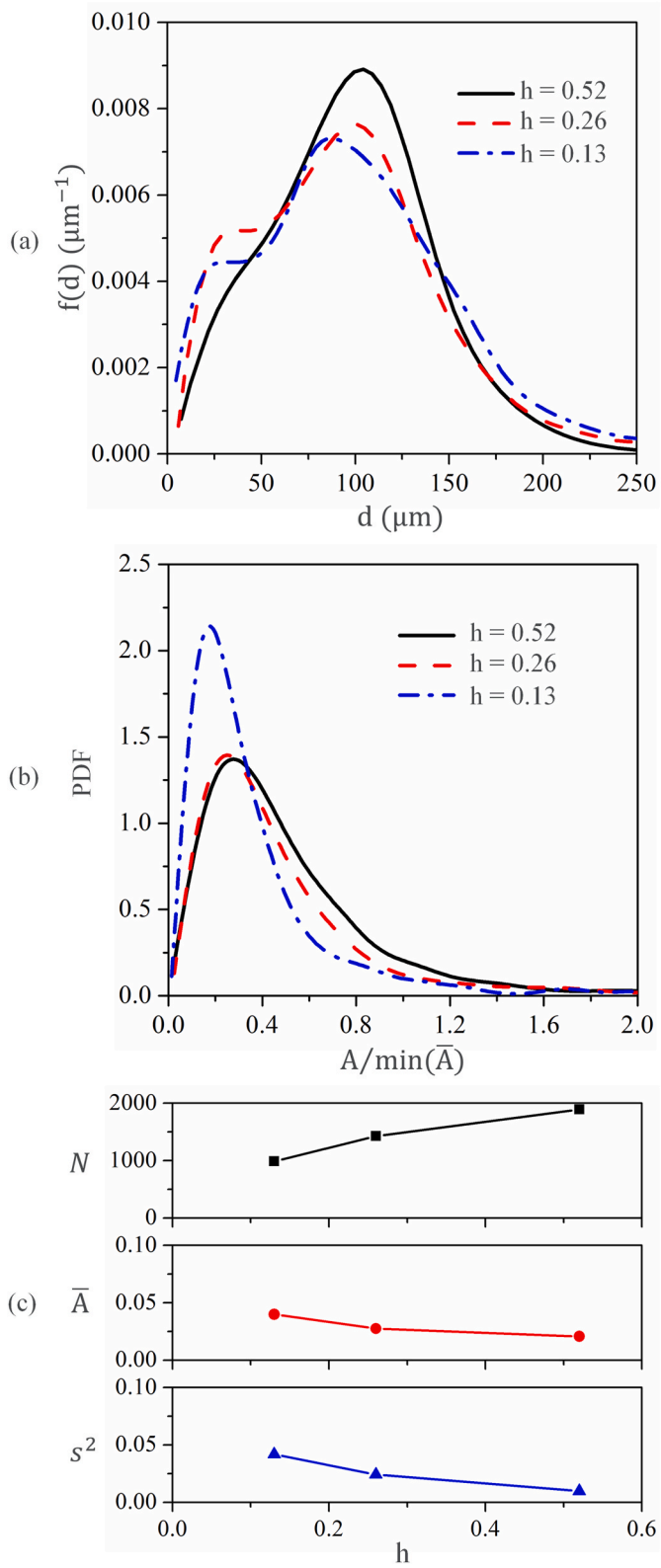

Fig. 11. Comparison of (a) PDF of discrete droplets diameter, (b) PDF of Voronoi volumes, and (c) the number, mean Voronoi volume, and square deviation for different film thicknesses h that shown in Fig. 10.

and nonuniformity of spray spatial distribution.

4.2. Effects of film width

Fig. 12 shows the SMD contour and Voronoi diagram for different film widths but the fixed film thickness. The transition from jet-film to modified jet-jet injection element is achieved by decreasing the film width w, and the continuous annular flow is thereby blocked to be several independent modified jet flows that one-by-one correspond to the radial jet flows. Again, as reducing mass flow rate by decreasing the film width, the 100%, 50%, and 25% throttleable levels in Fig. 12(a–c) respectively correspond to the local momentum ratio LMR of 2.24, 1.58, and 1.12, resulting in a decrease of the spray angle from about 70° in Fig. 12(a) to approximately 45° in Fig. 12(c), which is quite close to the empirical and optimal spray angle. This is because, in that situation with a fixed film thickness, the effective impact inertia of the film is approximately unchanged however the effective jet-film collision is enhanced because the jet diameter is decreased with the mass flow rate. The region area of nonzero SMD contour is reduced owing to the decrease in mass flow rate. In addition, owing to the enhanced effective impact between jet and film, apart from the axial direction for the film or the radial direction for the jet, the impact inertia can be also distributed along the resultant force direction, leading to the dispersed droplets showing a relatively uniform distribution.

To further characterize the spatial characteristics of sprays with varying mass flow rates, Fig. 13 quantitatively shows the PDF of discrete droplet diameters, PDF of Voronoi volumes, and the number, mean Voronoi volume, and square deviation for different film widths. A prominent finding is that there are no substantial differences between the PDF of droplet diameter and Voronoi volumes as decreasing the film width w, indicating the spray angle or the spatial spray characteristics are insensitive to the variation of film width for different throttleable levels, which is convenient and preferable for the design of throttleable engines. It is seen that the number of dispersed droplets decreases and the square deviation of Voronoi volumes increases as decreasing the film width w, leading to enhanced nonuniformity of droplet distribution. However, the square deviation value for $w = 3.75$ mm at 25% throttleable level is about 0.03 and prominently smaller than that for $h = 0.13$ mm of 0.05, indicating the uniformity of droplet distribution of the former is better. Thus, it is concluded that the strategy of decreasing film width is superior to decreasing film thickness for variable mass flow rate conditions, owing to the improved uniformity of droplet distribution and approximately insensitive spray angle and SMD distribution for different throttleable levels.

5. Conclusion

The present paper numerically studied the spray characteristics of a simplified jet-film injection element. Compared to the film-film injection element, it presents the non-uniform distribution of dispersed droplets where the dense spray occurs around the jet and the jet-film interaction region and the dilute spray is distributed after the jet and other film regions without impacting with the jet, showing a non-monotonic variation of spray contour along the spanwise of liquid film and prominent local characteristics of droplet clustering.

To quickly prescreen designs of pintle injectors, the present numerical study analyzed the spray characteristics based on both the Sauter Mean Diameter contour and the Voronoi tessellation. The results show that there is no prominent correlation between Sauter Mean Diameter and Voronoi volumes, but they reflect two different aspects of the spray. The Sauter Mean Diameter contour reflects the time average of discrete droplets at a certain spatial location, whereas the Voronoi cells reflect the local characteristics of discrete droplet distribution at a certain time. Thus, apart from the Sauter Mean Diameter substantially used in spray studies, the Voronoi tessellation characterizing the droplet clustering effects is also significant for the analysis of spray characteristics and the

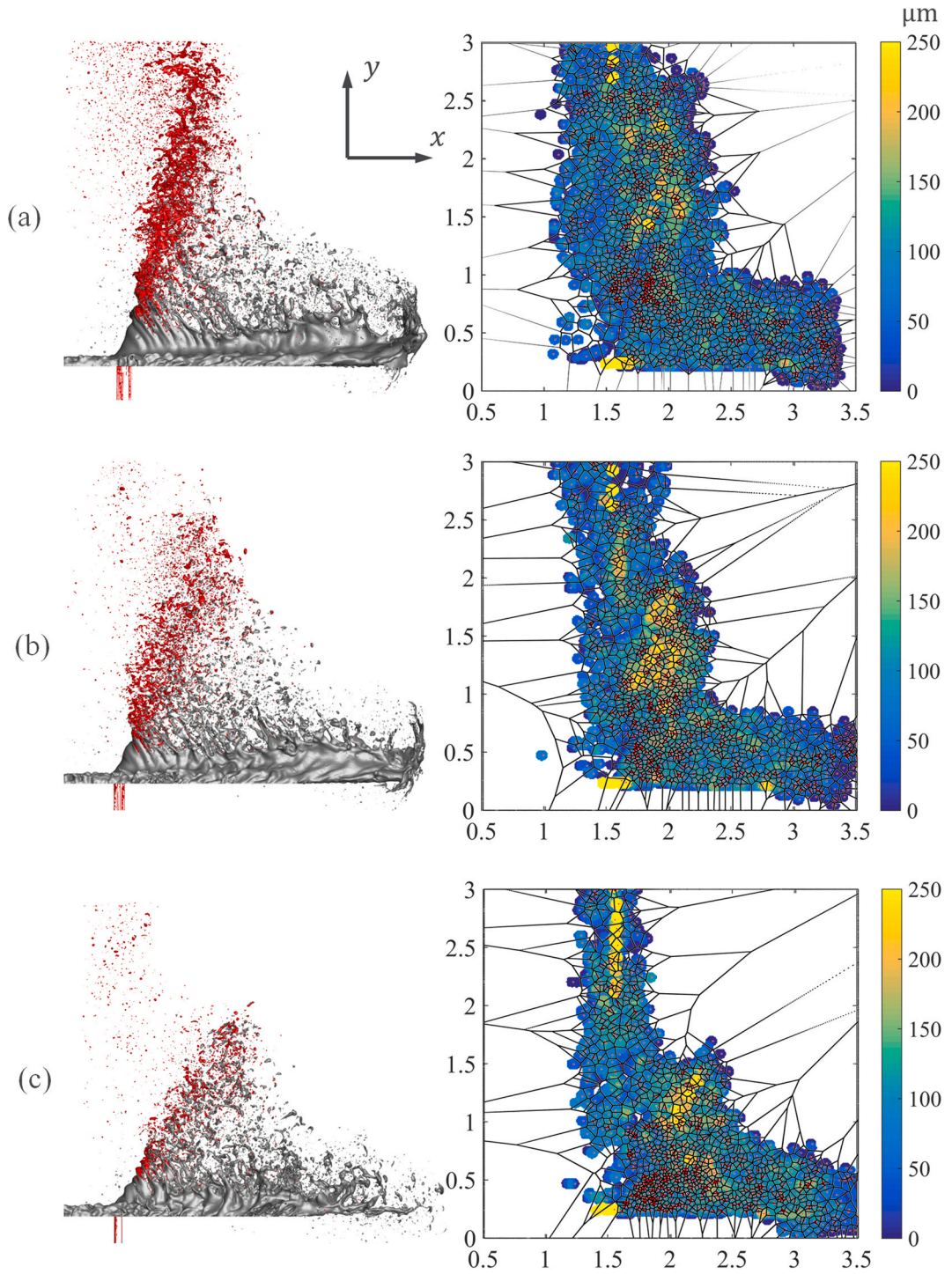

Fig. 12. Comparison of spray characteristics and overlapped SMD contour and Voronoi diagram at $z = 0.0$ for different film widths (a) $w = 15$ mm at 100% throttleable level, (b) $w = 7.5$ mm at 50% throttleable level, and (c) $w = 3.75$ mm at 25% throttleable level, with fixed $h = 0.52$ mm as decreasing the mass flow rate.

model of group combustion in sprays, which merits further study as an analysis method for the spray characteristics. The good spray characteristics tend to simultaneously have a small Sauter Mean Diameter but also a uniform distribution of Voronoi cells for all dispersed droplets.

Referring to the effects of film thickness and width on the spray characteristics of a jet-film injection element, it shows that decreasing film thickness leads to worse spray characteristics with increased spray angle and enhanced nonuniformity of droplet distribution, whereas decreasing film width can improve the uniformity of droplet distribution and approximately insensitive spray angle and droplet distribution for different throttleable levels, which is convenient and preferable for the design of throttleable engines. For a real pintle injector, the transition from jet-film to modified jet-jet injection element is achieved by decreasing the film width, and the continuous annular flow is thereby blocked to be several independent modified jet flows that one-by-one correspond to the radial jet flows. Thus, the numerical finding in the present paper verified a design concept that adopts traditional jet-film injection at a large mass flow rate and modified jet-jet injection at a small mass flow rate to maintain good spray performance during the entire throttleable levels.

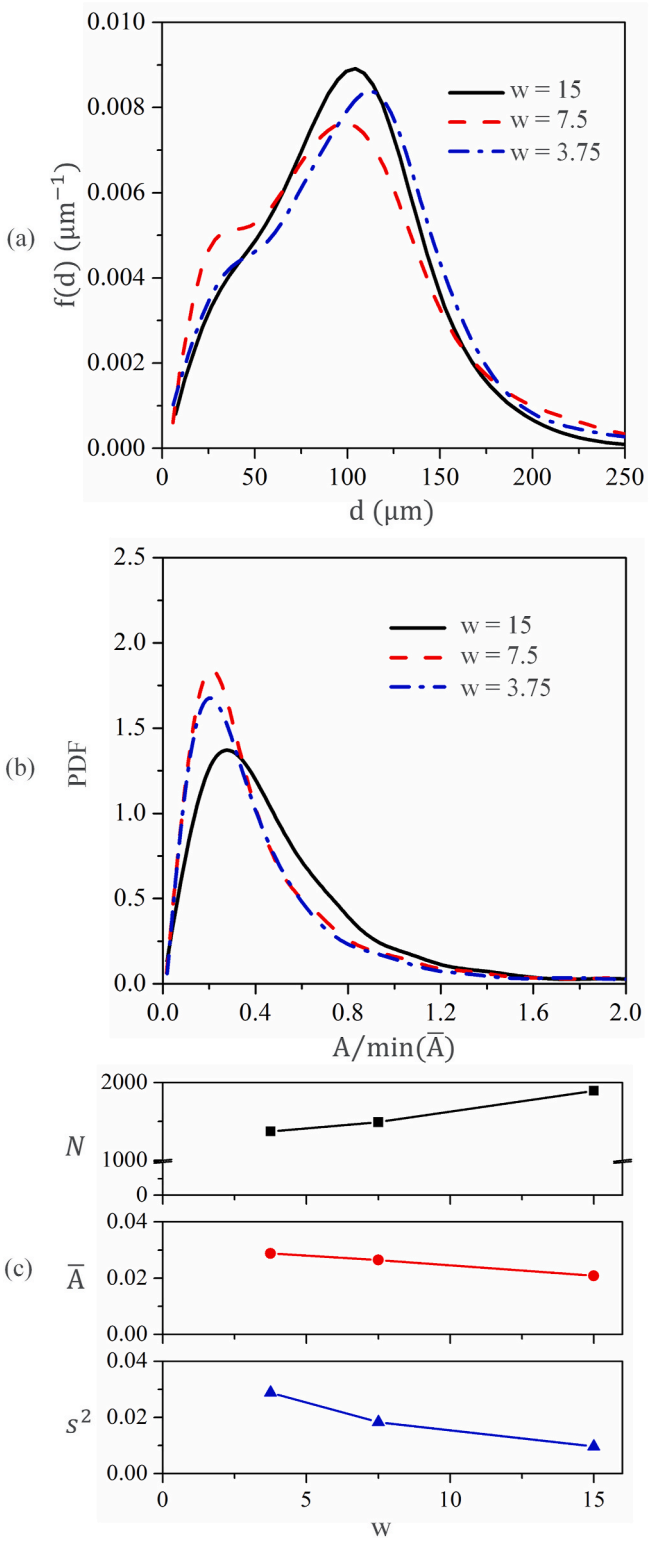

Fig. 13. Comparison of (a) PDF of discrete droplets diameter, (b) PDF of Voronoi volumes, and (c) the number, mean Voronoi volume, and square deviation for different film widths w that shown in Fig. 12.

Declaration of competing interest

The authors declare that they have no known competing financial interests or personal relationships that could have appeared to influence the work reported in this paper.

Acknowledgments

This work was supported by National Science Foundation of China (Grant No. 12102437, Grant No. 52176134, and Grant No. U2141220). The work at City University of Hong Kong was partially supported by a grant from the Research Grants Council of the Hong Kong Special Administrative Region, China (Project No. CityU15222421).

References

[1] E. Betts, R. Frederick, A historical systems study of liquid rocket engine throttling capabilities, in: 46th AIAA/ASME/SAE/ASEE Joint Propulsion Conference & Exhibit, 2010.
[2] M.J. Casiano, J.R. Hulka, V. Yang, Liquid-propellant rocket engine throttling: a comprehensive review, J. Propul. Power 26 (2010) 897–923.
[3] Z. Dong, M. Sun, Z. Wang, J. Chen, Z. Cai, Survey on key techniques of rocket-based combined-cycle engine in ejector mode, Acta Astronaut. 164 (2019) 51–68.
[4] W. Huang, Y. Xing, A conceptual study of RBCC for hypersonic missile, in: 41st AIAA/ASME/SAE/ASEE Joint Propulsion Conference & Exhibit, 2005.
[5] S. Heister, Pintle injectors, in: Handbook of Atomization and Sprays, Springer, 2011, pp. 647–655.
[6] T.J. Kelly, Moon Lander, How We Developed the Apollo Lunar Module, Smithsonian Institution, 2009.
[7] G. Dressler, J. Bauer, TRW pintle engine heritage and performance characteristics, in: 36th AiAA/ASME/SAE/ASEE Joint Propulsion Conference and Exhibit, 2000.
[8] B. Erkal, B. Sümer, M.H. Aksel, Design procedure and cold flow experiments of a pintle injector, in: AIAA Propulsion and Energy 2019 Forum, 2019.
[9] M. Son, K. Radhakrishnan, J. Koo, O.C. Kwon, H.D. Kim, Design Procedure of a movable pintle injector for liquid rocket engines, J. Propul. Power 33 (2017) 858–869.
[10] M. Son, K. Yu, J. Koo, O.C. Kwon, J.S. Kim, Effects of momentum ratio and weber number on spray half angles of liquid controlled pintle injector, J. Therm. Sci. 24 (2015) 37–43.
[11] P. Cheng, Q. Li, H. Chen, Flow characteristics of a pintle injector element, Acta Astronaut. 154 (2019) 61–66.
[12] P. Cheng, Q. Li, S. Xu, Z. Kang, On the prediction of spray angle of liquid-liquid pintle injectors, Acta Astronaut. 138 (2017) 145–151.
[13] S. Lee, D. Kim, J. Koo, Y. Yoon, Spray characteristics of a pintle injector based on annular orifice area, Acta Astronaut. 167 (2020) 201–211.
[14] S. Heo, D. Hwan Kim, I. Kim, Y. Yoon, Effects of grooved pintle tip applied to a gas–liquid pintle injector, in: Asia-Pacific International Symposium on Aerospace Technology, Springer, 2023.
[15] S. Heo, D.H. Kim, Y. Yoon, Effects of groove structure on spray characteristics of a throttleable pintle injector, J. Propul. Power (2022) 1–12.
[16] S. Erazo, J.A. Day, J. Gamertsfelder, P. Khare, J.M. Quinlan, Pintle injector spray atomization: liquid sheet breakup quantification, in: AIAA Propulsion and Energy 2021 Forum, 2021.
[17] X. Fang, C. Shen, Study on atomization and combustion characteristics of LOX/methane pintle injectors, Acta Astronaut. 136 (2017) 369–379.
[18] F. Zhao, H. Zhang, H. Zhang, B. Bai, L. Zhao, Review of atomization and mixing characteristics of pintle injectors, Acta Astronaut. 200 (2022) 400–419.
[19] J. Lux, O. Haidn, Flame stabilization in high-pressure liquid oxygen/methane rocket engine combustion, J. Propul. Power 25 (2009) 15–23.
[20] K. Sakaki, T. Funahashi, S. Nakaya, M. Tsue, R. Kanai, K. Suzuki, T. Inagawa, T. Hiraiwa, Longitudinal combustion instability of a pintle injector for a liquid rocket engine combustor, Combust. Flame 194 (2018) 115–127.
[21] V. Betelin, N. Smirnov, V. Nikitin, V. Dushin, A. Kushnirenko, V. Nerchenko, Evaporation and ignition of droplets in combustion chambers modeling and simulation, Acta Astronaut. 70 (2012) 23–35.
[22] N. Smirnov, V. Betelin, A. Kushnirenko, V. Nikitin, V. Dushin, V. Nerchenko, Ignition of fuel sprays by shock wave mathematical modeling and numerical simulation, Acta Astronaut. 87 (2013) 14–29.
[23] N. Smirnov, V. Nikitin, J. Khadem, S. Alyari-Shourekhdeli, Onset of detonation in polydispersed fuel–air mixtures, Proc. Combust. Inst. 31 (2007) 2195–2204.
[24] N. Smirnov, V. Nikitin, V. Dushin, Y. Filippov, V. Nerchenko, J. Khadem, Combustion onset in non-uniform dispersed mixtures, Acta Astronaut. 115 (2015) 94–101.
[25] K. Radhakrishnan, M. Son, K. Lee, J. Koo, Effect of injection conditions on mixing performance of pintle injector for liquid rocket engines, Acta Astronaut. 150 (2018) 105–116.
[26] N. Ashgriz, Handbook of Atomization and Sprays: Theory and Applications, Springer Science & Business Media, 2011.
[27] H. Wu, F. Zhang, Z. Zhang, Droplet breakup and coalescence of an internal-mixing twin-fluid spray, Phys. Fluids 33 (2021), 013317.
[28] C. Liu, K. Wu, Z. Zhang, Y. Yuan, X. Fan, Experimental study of the spray characteristics of twin-fluid atomization: focusing on the annular flow regime, Phys. Fluids 34 (2022), 123309.
[29] C. Zhang, Z. Zhang, K. Wu, X. Xia, X. Fan, Atomization ofmisaligned impinging liquid jets, Phys. Fluids 33 (2021), 093311.
[30] H. Chiu, R. Ahluwalia, E. Croke, Spray Group Combustion, 16th Aerospace Sciences Meeting, 1978.
[31] H. Chiu, T. Liu, Group combustion of liquid droplets, Combust. Sci. Technol. 17 (1977) 127–142.

[32] J. Urzay, A revised spray-combustion diagram of diffusion-controlled burning regimes in fuel-spray clouds, Annu. Res. Briefs, Cent. Turbul. Res. Stanford Univ (2011) 193–198.
[33] V. Boddapati, M. Manish, S. Sahu, A novel approach for conditional measurement of droplet size distribution within droplet clusters in sprays, Exp. Fluid 61 (2020) 1–17.
[34] M. Manish, S. Sahu, Optical characterization of droplet clusters and group combustion in spray diffusion flames, Proc. Combust. Inst. 38 (2021) 3409–3416.
[35] S. Sahu, Analysis of droplet clustering in air-assist sprays using Voronoi tessellations, Phys. Fluids 30 (2018), 123305.
[36] F. Salvador, S. Ruiz, M. Crialesi-Esposito, I. Blanquer, Analysis on the effects of turbulent inflow conditions on spray primary atomization in the near-field by direct numerical simulation, Int. J. Multiphas. Flow 102 (2018) 49–63.
[37] J. Shinjo, A. Umemura, Detailed simulation of primary atomization mechanisms in diesel jet sprays (isolated identification of liquid jet tip effects), Proc. Combust. Inst. 33 (2011) 2089–2097.
[38] F. Gibou, R. Fedkiw, S. Osher, A review of level-set methods and some recent applications, J. Comput. Phys. 353 (2018) 82–109.
[39] T. Ménard, S. Tanguy, A. Berlemont, Coupling level set/VOF/ghost fluid methods: validation and application to 3D simulation of the primary break-up of a liquid jet, Int. J. Multiphas. Flow 33 (2007) 510–524.
[40] S. Popinet, Numerical models of surface tension, Annu. Rev. Fluid Mech. 50 (2018) 49–75.
[41] H. Grosshans, R.Z. Szász, L. Fuchs, Development of an efficient statistical volumes of fluid–Lagrangian particle tracking coupling method, Int. J. Numer. Methods Fluid. 74 (2014) 898–918.
[42] G. Tomar, D. Fuster, S. Zaleski, S. Popinet, Multiscale simulations of primary atomization, Comput. Fluids 39 (2010) 1864–1874.
[43] X. Chen, V. Yang, Recent advances in physical understanding and quantitative prediction of impinging-jet dynamics and atomization, Chin. J. Aeronaut. 32 (2019) 45–57.
[44] T. Zaripov, A. Gilfanov, S. Begg, O. Rybdylova, S. Sazhin, M. Heikal, The fully Lagrangian approach to the analysis of particle/droplet dynamics: implementation into ansys fluent and application to gasoline sprays, Atomization Sprays 27 (2017).
[45] X. Li, M. Soteriou, High fidelity simulation and analysis of liquid jet atomization in a gaseous crossflow at intermediate Weber numbers, Phys. Fluids 28 (2016), 082101.
[46] S. Popinet, Gerris: a tree-based adaptive solver for the incompressible Euler equations in complex geometries, J. Comput. Phys. 190 (2003) 572–600.
[47] S. Popinet, An accurate adaptive solver for surface-tension-driven interfacial flows, J. Comput. Phys. 228 (2009) 5838–5866.
[48] X. Chen, D. Ma, V. Yang, S. Popinet, High-fidelity simulations of impinging jet atomization, Atomization Sprays 23 (2013).
[49] X. Yang, A. Turan, Simulation of liquid jet atomization coupled with forced perturbation, Phys. Fluids 29 (2017), 022103.
[50] D. Fuster, A. Bagué, T. Boeck, L. Le Moyne, A. Leboissetier, S. Popinet, P. Ray, R. Scardovelli, S. Zaleski, Simulation of primary atomization with an octree adaptive mesh refinement and VOF method, Int. J. Multiphas. Flow 35 (2009) 550–565.
[51] D. Fuster, J. Matas, S. Marty, S. Popinet, J. Hoepffner, A. Cartellier, S. Zaleski, Instability regimes in the primary breakup region of planar coflowing sheets, J. Fluid Mech. 736 (2013) 150–176.
[52] P. Zhang, B. Wang, Effects of elevated ambient pressure on the disintegration of impinged sheets, Phys. Fluids 29 (2017), 042102.
[53] H. Grosshans, A. Movaghar, L. Cao, M. Oevermann, R.-Z. Szász, L. Fuchs, Sensitivity of VOF simulations of the liquid jet breakup to physical and numerical parameters, Comput. Fluids 136 (2016) 312–323.
[54] N. Smirnov, V. Betelin, V. Nikitin, L. Stamov, D. Altoukhov, Accumulation of errors in numerical simulations of chemically reacting gas dynamics, Acta Astronaut. 117 (2015) 338–355.
[55] N. Smirnov, V. Betelin, R. Shagaliev, V. Nikitin, I. Belyakov, Y.N. Deryuguin, S. Aksenov, D. Korchazhkin, Hydrogen fuel rocket engines simulation using LOGOS code, Int. J. Hydrogen Energy 39 (2014) 10748–10756.
[56] J. Eggers, E. Villermaux, Physics of liquid jets, Rep. Prog. Phys. 71 (2008), 036601.
[57] C. Josserand, S.T. Thoroddsen, Drop impact on a solid surface, Annu. Rev. Fluid Mech. 48 (2016) 365–391.
[58] S. Haefner, M. Benzaquen, O. Bäumchen, T. Salez, R. Peters, J.D. McGraw, K. Jacobs, E. Raphaël, K. Dalnoki-Veress, Influence of slip on the Plateau–Rayleigh instability on a fibre, Nat. Commun. 6 (2015) 7409.
[59] F. Aurenhammer, Voronoi diagrams—a survey of a fundamental geometric data structure, ACM Comput. Surv. 23 (1991) 345–405.
[60] L. Mu, Polygon characterization with the multiplicatively weighted Voronoi diagram, Prof. Geogr. 56 (2004) 223–239.